Topological Axion States in the Magnetic Insulator $MnBi_2Te_4$ with the Quantized Magnetoelectric Effect

Dongqin Zhang,[1] Minji Shi,[1] Tongshuai Zhu,[1] Dingyu Xing,[1,2] Haijun Zhang,[1,2,*] and Jing Wang[3,2,4,†]
[1]National Laboratory of Solid State Microstructures, School of Physics, Nanjing University, Nanjing 210093, China
[2]Collaborative Innovation Center of Advanced Microstructures, Nanjing University, Nanjing 210093, China
[3]State Key Laboratory of Surface Physics, Department of Physics, Fudan University, Shanghai 200433, China
[4]Institute for Nanoelectronic Devices and Quantum Computing, Fudan University, Shanghai 200433, China

(Received 18 September 2018; revised manuscript received 24 January 2019; published 20 May 2019)

Topological states of quantum matter have attracted great attention in condensed matter physics and materials science. The study of time-reversal-invariant topological states in quantum materials has made tremendous progress. However, the study of magnetic topological states falls much behind due to the complex magnetic structures. Here, we predict the tetradymite-type compound $MnBi_2Te_4$ and its related materials host topologically nontrivial magnetic states. The magnetic ground state of $MnBi_2Te_4$ is an antiferromagetic topological insulator state with a large topologically nontrivial energy gap (~0.2 eV). It presents the axion state, which has gapped bulk and surface states, and the quantized topological magnetoelectric effect. The ferromagnetic phase of $MnBi_2Te_4$ might lead to a minimal ideal Weyl semimetal.

DOI: 10.1103/PhysRevLett.122.206401

The discovery of time-reversal-invariant (TRI) topological insulators (TIs) [1–4] brings the opportunity to realize a large family of exotic topological phenomena through magnetically gapping the topological surface states (SSs) [5–36]. Tremendous efforts have been made to introduce magnetism into TRI TIs. One successful example is the first realization of the quantum anomalous Hall (QAH) effect in Cr-doped $(Bi, Sb)_2Te_3$ TI thin films [28,37,38]. Aside from the dilute magnetic TIs, intrinsic magnetic materials are expected to provide a clean platform to study magnetic topological states with new interesting topological phenomena. Some magnetic topological states have been theoretically proposed [39], such as antiferromagnetic (AFM) TI [29], a dynamical axion field [40], magnetic Dirac semimetals [32,33,41,42], and Weyl semimetals [30,31,43]. Though a few magnetic Weyl semimetals were experimentally observed [44], the study of magnetic topological states falls much behind in experiments due to complex magnetic structure. Therefore, realistic intrinsic magnetic topological materials are highly desired. The class of $MnBi_2Te_4$ materials predicted in this Letter provide an ideal platform for emergent magnetic topological phenomena, such as AFM TI, topological axion state with quantized topological magnetoelectric effect (TME), minimal ideal Weyl semimetal, QAH effect, two-dimensional ferromagnetism, and so on.

The tetradymite-type compounds XA_2B_4, also written as XBA_2B_3 with X = Ge, Sn, Pb or Mn, A = Sb or Bi, and B = Se or Te, crystallize in a rhombohedral crystal structure with the space group D^5_{3d} (No. 166) with seven atoms in one unit cell. We take $MnBi_2Te_4$ as an example, which has been successfully synthesized in experiments [45]. It has layered structures with a triangle lattice, shown in Fig. 1. The trigonal axis (threefold rotation symmetry C_{3z}) is defined as the z axis, a binary axis (twofold rotation symmetry C_{2x}) is defined as the x axis and a bisectrix axis (in the reflection plane) is defined as the y axis for the coordinate system. The material consists of seven-atom layers (e.g., Te1-Bi1-Te2-Mn-Te3-Bi2-Te4) arranged along the z direction, known as a septuple layer (SL), which could

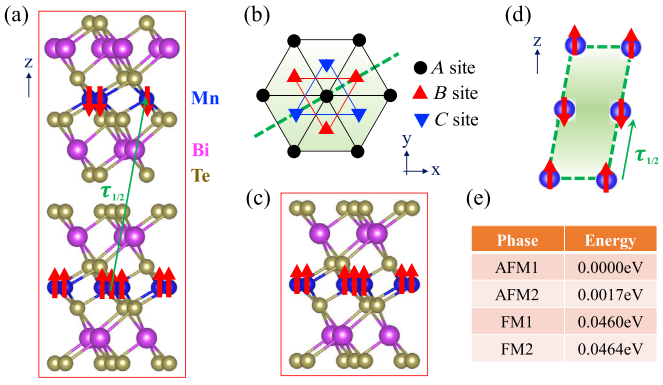

Phase	Energy
AFM1	0.0000eV
AFM2	0.0017eV
FM1	0.0460eV
FM2	0.0464eV

FIG. 1. Crystal structure and magnetic structure. (a) The unit cell of AFM $MnBi_2Te_4$ consists of two SLs. The red arrows represent the spin moment of Mn atom. The green arrow denotes for the half translation operator $\tau_{1/2}$. (b) Schematic top view along the z direction. The triangle lattice in one SL has three different positions, denoted as A, B, and C. The dashed green line is used for the (011) plane. (c) The unit cell of FM $MnBi_2Te_4$ has one SL. (d) The schematic of the (011) plane, with the blue balls denoting Mn atoms. (e) The calculated total energy for different magnetic ordered states.

be simply viewed as the intergrowth of (111) plane of rock-salt structure MnTe within the quintuple layer of TI Bi_2Te_3 [see Fig. 1(a) and (c)] [10]. The coupling between different SLs is the van der Waals type. The existence of inversion symmetry $\mathcal{I}$, with the Mn site as the inversion center, enables us to construct eigenstates with definite parity.

First-principles calculations are employed to investigate the electronic structure of $MnBi_2Te_4$, where the detailed methods can be found in the Supplemental Material [46]. We find that each Mn atom in $MnBi_2Te_4$ tends to have half-filled d orbitals. We performed total energy calculations for different magnetic phases for the three-dimensional $MnBi_2Te_4$, and the results are listed in Fig. 1(e), showing that the A-type AFM phase with the out-of-plane easy axis, denoted as AFM1 [seen in Fig. 1(a)], is the magnetic ground state. It is ferromagnetic (FM) within the xy plane in each SL, and AFM between neighbor SLs along the z direction, consisting with the previous report [49]. The total energy of the A-type AFM phase AFM2 with the in plane easy axis is slightly higher than that of AFM1, and much lower than that of FM phase FM1 with the out of plane easy axis, which indicates that the magnetic anisotropy is weaker than the effective magnetic exchange interaction between Mn atoms in neighbor SLs. The FM phase FM2 with in plane easy axis has the highest energy. The Goodenough-Kanamori rule is the key to understand the AFM1 ground state. For the in plane Mn atomic layer, two nearest Mn atoms are connected through Te atom with the bond "Mn—Te—Mn," whose bonding angle is close to 90 degree, so the superexchange interaction is expected to induce FM ordering. Contrarily, Mn atoms between neighbor atomic layers are coupled through the bond "Mn—Te—Bi—Te:Te—Bi—Te—Mn," considered as an effective bond "Mn—X—Mn" with a 180 degree bonding angle, where AFM ordering is induced. In the following discussion, we would focus on the AFM1 (the magnetic ground state) and FM1 (possibly realized through an external magnetic field) states.

First, we investigate the AFM1 ground state. The band structures without and with spin-orbit coupling (SOC) are shown in Figs. 2(a) and 2(b), respectively. The time-reversal symmetry Θ is broken; however, a combined symmetry $\mathcal{S} = \Theta\tau_{1/2}$ is preserved, where $\tau_{1/2}$ is the half translation operator connecting nearest spin-up and -down Mn atomic layers, marked in Fig. 1(a). The operator $\mathcal{S}$ is antiunitary with $\mathcal{S}^2 = -e^{-i\mathbf{k}\cdot\tau_{1/2}}$. $\mathcal{S}^2 = -1$ on the Brillouin-zone (BZ) plane $\mathbf{k}\cdot\tau_{1/2} = 0$. Therefore, similar to Θ in TRI TI, $\mathcal{S}$ could also lead to a $\mathcal{Z}_2$ classification [29], where the topological invariant is well defined on the BZ plane with $\mathbf{k}\cdot\tau_{1/2} = 0$. One can see an anticrossing feature around the Γ point from the band inversion, suggesting that $MnBi_2Te_4$ might be topologically nontrivial. Since $\mathcal{I}$ is still preserved, the $\mathcal{Z}_2$ invariant is simply determined by the parity of the wave functions at TRI momenta (TRIM) in the Brillouin zone [50]. Here we only need consider the four

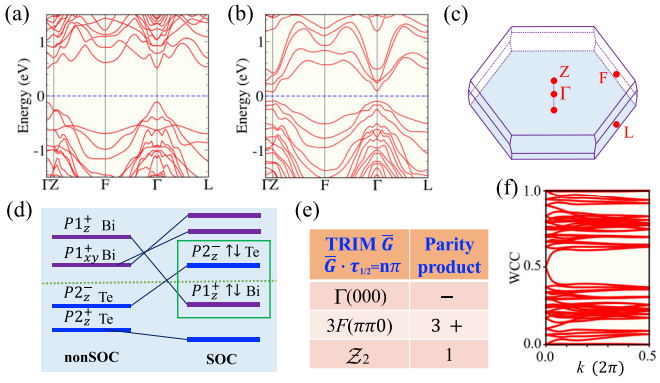

FIG. 2. Electronic structure of AFM1 $MnBi_2Te_4$. (a) and (b) The band structure of AFM1 state without (a) and with (b) SOC. (b) The bands are twofold degenerate due to conserved $\mathcal{I}$ and $\mathcal{S}$. (c) Brillouin zone of $MnBi_2Te_4$. The four inequivalent TRIM are $\Gamma(0,0,0)$, $L(\pi,0,0)$, $F(\pi,\pi,0)$, and $Z(\pi,\pi,\pi)$. (d) Schematic diagram of the band inversion at Γ. The green dotted line represents the Fermi level. (e) The parity product at the TRIM with $\bar{\mathbf{G}}\cdot\tau_{1/2} = n\pi$. (f) The Wannier charge centers (WCC) is calculated in the plane with Γ and $3F$, confirming $\mathcal{Z}_2 = 1$.

TRIM (Γ and three F) with $\bar{\mathbf{G}}\cdot\tau_{1/2} = n\pi$. As expected, by turning on SOC, the parity of one occupied band is changed at Γ point from band inversion between the $|P1_z^+\rangle$ of Bi and the $|P2_z^-\rangle$ of Te, schematically shown in Fig. 2(d), whereas the parity remains unchanged for all occupied bands at the other three momenta F [see Fig. 2(e)], so $\mathcal{Z}_2 = 1$. We also employ the Willson loop method [51] to confirm the $\mathcal{Z}_2$ invariant in Fig. 2(f), concluding that AFM $MnBi_2Te_4$ is an AFM TI. Especially, we notice that a large energy gap of about 0.2 eV is obtained in Fig. 2(b).

The existence of topological SSs is one of the most important properties of TIs. However, the TI state in AFM $MnBi_2Te_4$ protected by $\mathcal{S}$ is topological in a weaker sense than the strong TI protected by Θ, which manifests in that the existence of gapless SS depends on the surface plane. As shown in Figs. 4(a) and 4(c), there is gapped SSs on the (111) surface accompanied by a triangular Fermi surface, for $\mathcal{S}$ is broken. As shown in Fig. 4(b), only on the $\mathcal{S}$-preserving surfaces such as (011) surface, the gapless SSs are topologically protected which forms a single Dirac-cone-type dispersion at Γ.

For the FM1 state of $MnBi_2Te_4$, the band structures without and with SOC effect are shown in Fig. 3. $MnBi_2Te_4$ is a FM insulator with the experimental lattice constant (a_0, c_0), shown in Fig. 3(b). Interestingly, we find that the band structure is sensitive to the lattice constant. When the lattice constant is slightly extended, it first becomes a type-II Weyl semimetal with $(1.005a_0, 1.005c_0)$ and then becomes a minimal ideal Weyl semimetal with $(1.01a_0, 1.01c_0)$, hosting two Weyl points at the Fermi level without other bulk bands mixing, shown in Figs. 3(c) and 3(d). The Willson loop calculations, shown in Figs. 3(e) and 3(f), suggest that the Chern number $C = 1$ at $k_z = 0$ plane, and $C = 0$ at

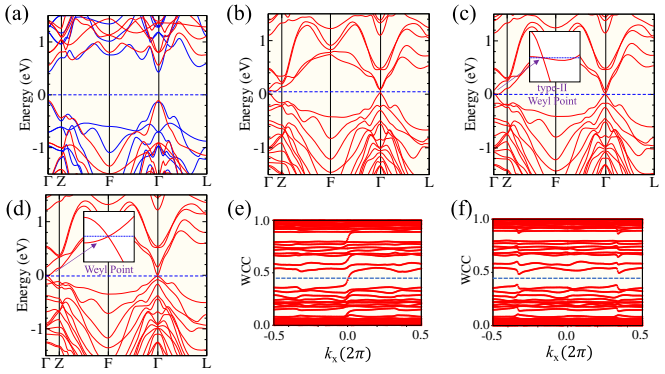

FIG. 3. Electronic structure of FM1 $MnBi_2Te_4$. (a) Band structure for FM1 state without SOC. The dashed line indicates the Fermi level. The red (blue) lines are spin-up (-down) bands. (b)–(d) Band structures for FM1 state with SOC are calculated by the LDA + U ($U = 3$ eV) functional with experimental lattice constants (a_0, c_0) in (b), extended lattice constants ($1.005a_0$, $1.005c_0$) in (c) and ($1.01a_0$, $1.01c_0$) in (d), respectively. The system has the transition from FM insulator to type-II Weyl semimetal, and finally to ideal Weyl semimetal. (e) and (f) The evolution of WCC along the k_x direction in the $k_z = 0$ plane (e) and in the $k_z = \pi$ plane (f). The WCCs cross the reference horizontal line once in (e), indicating the Chern number $C = 1$ in the $k_z = 0$ plane. Oppositely, the WCCs don't cross the reference line in (f), indicating the Chern number $C = 0$ in the $k_z = \pi$ plane.

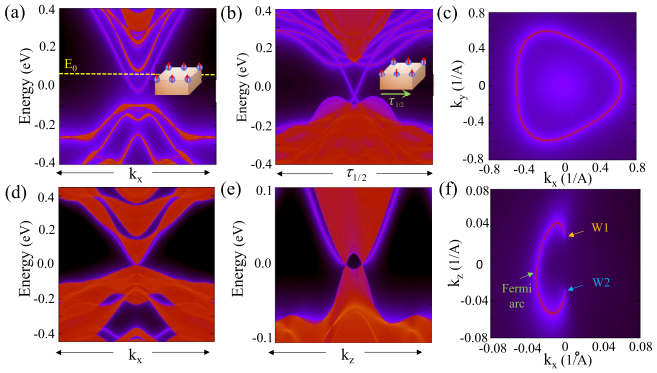

FIG. 4. Surface states. (a) and (b) Energy and momentum dependence of the local density of states (LDOS) for AFM1 phase on the (111) and (011) surfaces, respectively. In (a), The SSs on (111) surface are fully gapped due to the $\mathcal{S}$ symmetry broken. In (b), The gapless SSs can be seen at the Γ point with a linear dispersion in the bulk gap on the $\mathcal{S}$-preserving (011) surface. (c) Fermi surface on the (111) surface at the energy level E_0 in (a) presents the triangle shape, different from the hexagonal shape in TI Bi_2Se_3. (d) and (e), Energy and momentum dependence of the LDOS for FM1 phase on the (111) and (011) surfaces, respectively. In (e), the two Weyl points are seen along the k_z direction. (f) There are two Fermi arc connecting the Weyl points W1 and W2, indicating the ideal Weyl semimetal feature.

$k_z = \pi$ plane, which is consist with the ideal Weyl semimetal in Fig. 3(d). Furthermore, the SSs of FM1 state on different typical surfaces are calculated. In Fig. 4(d), bulk states projected on the (111) surface have no energy gap, for the two Weyl points are exactly projected to the surface $\bar{\Gamma}$ point. In Fig. 4(e) and 4(f), one can clearly see the surface Fermi arcs connecting to the two ideal Weyl points are separated ($\sim$0.06 Å^{-1}).

Low-energy effective model.—As the topological nature is determined by the physics near the Γ point, a simple effective Hamiltonian can be written down to characterize the low-energy long-wavelength properties of the system. We start from the four low-lying states $|P1_z^+, \uparrow(\downarrow)\rangle$ and $|P2_z^-, \uparrow(\downarrow)\rangle$ at the Γ point. Here the superscripts "+," "−" stand for the parity of the corresponding states. Without the SOC effect, around the Fermi energy, the bonding state $|P1_z^+\rangle$ of two Bi layers stays above of the antibonding state $|P2_z^-\rangle$ of two Te layers (Te1 and Te4 in SLs). As shown in Fig. 2(d), the SOC mixes spin and orbital angular momenta while preserving the total angular momentum, and $|P1_z^+, \uparrow(\downarrow)\rangle$ state is pushed down and the $|P2_z^-, \uparrow(\downarrow)\rangle$ state is pushed up, leading to the band inversion and parity exchange. In the nonmagnetic state, the symmetries of the system are Θ, $\mathcal{I}$, C_{3z} and C_{2x}. In the basis of ($|P1_z^+, \uparrow\rangle$, $|P2_z^-, \uparrow\rangle$, $|P1_z^+, \downarrow\rangle$, $|P2_z^-, \downarrow\rangle$), the representation of symmetry operations is given by $\Theta = 1_{2\times2} \otimes i\sigma^y\mathcal{K}$, $\mathcal{I} = \tau^z \otimes 1_{2\times2}$, $C_{3z} = \exp[1_{2\times2} \otimes i(\pi/3)\sigma^z]$ and $C_{2x} = \exp[\tau^z \otimes i(\pi/2)\sigma^x]$, where $\mathcal{K}$ is the complex conjugation operator, and $\sigma^{x,y,z}$ and $\tau^{x,y,z}$ denote the Pauli matrices in the spin and orbital space, respectively. By requiring these four symmetries and keeping only the terms up to quadratic order in $\mathbf{k}$, we obtain the following generic form of the effective Hamiltonian for nonmagnetic state

$$\mathcal{H}_N(\mathbf{k}) = \epsilon_0(\mathbf{k}) + \begin{pmatrix} M_\gamma(\mathbf{k}) & A_1 k_z & 0 & A_2 k_- \\ A_1 k_z & -M_\gamma(\mathbf{k}) & A_2 k_- & 0 \\ 0 & A_2 k_+ & M_\gamma(\mathbf{k}) & -A_1 k_z \\ A_2 k_+ & 0 & -A_1 k_z & -M_\gamma(\mathbf{k}) \end{pmatrix},$$

where $k_\pm = k_x \pm ik_y$, $\epsilon_0(\mathbf{k}) = C + D_1 k_z^2 + D_2(k_x^2 + k_y^2)$, and $M_\gamma(\mathbf{k}) = M_0^\gamma + B_1^\gamma k_z^2 + B_2^\gamma(k_x^2 + k_y^2)$.

The FM1 state breaks Θ and C_{2x} but preserves the combined $C_{2x}\Theta$; therefore the effective Hamiltonian for FM1 is obtained by adding perturbative term $\delta\mathcal{H}_{\mathrm{FM1}}(\mathbf{k})$ respecting the corresponding symmetries into $\mathcal{H}_N(\mathbf{k})$, which is

$$\delta\mathcal{H}_{\mathrm{FM1}}(\mathbf{k}) = \begin{pmatrix} M_1(\mathbf{k}) & A_3 k_z & 0 & A_4 k_- \\ A_3 k_z & M_2(\mathbf{k}) & -A_4 k_- & 0 \\ 0 & -A_4 k_+ & -M_1(\mathbf{k}) & A_3 k_z \\ A_4 k_+ & 0 & A_3 k_z & -M_2(\mathbf{k}) \end{pmatrix},$$

where $M_{1,2}(\mathbf{k}) = M_\alpha(\mathbf{k}) \pm M_\beta(\mathbf{k})$, and $M_j(\mathbf{k}) = M_0^j + B_1^j k_z^2 + B_2^j(k_x^2 + k_y^2)$ with $j = \alpha, \beta$. By fitting the

energy spectrum of the effective Hamiltonian with that of the first-principles calculation, the parameters in the effective model can be determined, which can be found in the Supplemental Material [46]. The $M_{1,2}$ terms characterize the Zeeman coupling with the magnetized Mn orbitals, and in general $M_1 \neq M_2$ denotes the different effective g factor of $|P1_z^+, \uparrow(\downarrow)\rangle$ and $|P2_z^-, \uparrow(\downarrow)\rangle$.

The AFM1 state breaks Θ but preserves $\mathcal{S} = 1_{2\times 2} \otimes i\sigma^y \mathcal{K} e^{i\mathbf{k}\cdot\tau_{1/2}}$, and the unit cell doubles compared to FM1 state. For simplicity, we obtain the low-energy four-band model similar to the above analysis. From band structure analysis, the four bands close the Fermi energy in the AFM1 state are the new bonding state $|P1_z'^+, \uparrow(\downarrow)\rangle$ of four Bi layers and the antibonding state $|P2_z'^-, \uparrow(\downarrow)\rangle$ of four Te layers (two Te1 and two Te4 in neighboring SLs). In the basis of $(|P1_z'^+, \uparrow\rangle, |P2_z'^-, \uparrow\rangle, |P1_z'^+, \downarrow\rangle, |P2_z'^-, \downarrow\rangle)$, by requiring the symmetries $\mathcal{I}$, C_{3z}, and $\mathcal{S}$, we get the effective Hamiltonian for AFM1 which has the *same* expression as $\mathcal{H}_N(\mathbf{k})$ but with different parameters. The AFM1 model and fitting parameters are listed in the Supplemental Material [46].

Axion state and topological response.—The topological electromagnetic response from AFM TI is described by the topological θ term, $S_\theta = (\theta/2\pi)(\alpha/2\pi)\int d^3x dt \mathbf{E}\cdot\mathbf{B}$. Here, $\mathbf{E}$ and $\mathbf{B}$ are the conventional electromagnetic fields inside the insulator, $\alpha = e^2/\hbar c$ is the fine-structure constant, e is electron charge, and θ is dimensionless pseudoscalar parameter and defined only modulo 2π. Physically, θ has an explicit microscopic expression of the momentum space Chern-Simons form [34,52]. $\mathcal{S}$ constrains θ to be quantized, namely $\theta = -\theta + 2\pi n$ for integer n, thus $\theta = \pi$ for AFM TI. From the effective action with open boundary conditions, we know that $\theta = \pi$ implies a surface quantized Hall conductance of $\sigma_{xy} = e^2/2h$. This half quantized Hall effect on the surface is the physical origin behind the topological TME effect. For a finite TRI TI, Θ forces TME to vanish, where the surface and bulk states contribution to TME precisely cancel each other [34,53,54]. As is suggested in Refs. [34,55], to obtain the quantized TME in TIs, one must fulfill the following stringent requirements. First, all surfaces are gapped by magnetic ordering. Second, the Fermi level is finely tuned into the magnetically induced surface gap to keep the bulk truly insulating. Third, the film of TI material should be thick enough to eliminate the finite-size effect. However, the previous proposals on TME in the FM-TI heterostructure have several drawbacks. First, the gapless SSs on side surfaces are hard to eliminate [55–57], which will destroy the TME. Second, the surface gap is tiny due to weak magnetic proximity effect.

Interestingly, $MnBi_2Te_4$ provides a feasible platform for quantized TME, which has not been experimentally observed. One advantage is that the $\mathcal{S}$ breaking surfaces are gapped by material's own time-reversal breaking, thus allowing a nonvanishing TME. One can simply grow realistic materials without any $\mathcal{S}$-preserving surfaces or apply a small in plane magnetic field. Such axion state has fully gapped bulk and surfaces, and the same topological response as AFM TI with $\theta = \pi$. The second advantage is that the surface gap induced by intrinsic magnetism is large of about 0.1 eV. Furthermore, the finite-size effect is negligible when the film exceed 4 SLs [46]. Experimentally, such quantized TME can be observed by measuring the induction of a parallel polarization current when an ac magnetic field is applied [55], which is $\mathcal{J} = (\theta/\pi)(e^2/2h)(\partial B_x/\partial t)\ell d$. Here, d and ℓ are the thickness and width of the $MnBi_2Te_4$ sample. For an estimation, taking $B_x = B_0 e^{-i\omega t}$, $B_0 = 10$ G, $\omega/2\pi = 1$ GHz, $d = 50$ nm, $\theta = \pi$, and $\ell = 400$ μm, we have $\mathcal{J} = -i\mathcal{J}_0 e^{-i\omega t}$ with $\mathcal{J}_0 = 2.22$ nA, in the range accessible by experiments.

It is worth mentioning that the Néel order in AFM1 state is essentially different from that in dynamical axion field proposed in Ref. [40]. In the latter case, the Néel order breaks Θ and $\mathcal{I}$, but conserves $\mathcal{I}\Theta$. The magnetic fluctuation of the Néel order leads to linear contribution to the fluctuation of axion field, and the static θ deviates from π. While in the case of AFM1 $MnBi_2Te_4$, the Néel order conserves both $\mathcal{I}$ and $\mathcal{S}$, thus the static $\theta = \pi$, and to the linear order, the magnetic fluctuation has no contribution to the dynamics of axion field [40,58].

Materials.—Other tetradymite-type compounds XBi_2Te_4, XBi_2Se_4, and XSb_2Te_4 (X = Mn or Eu), if with the same rhombohedral crystal structure, are also promising candidates to host magnetic topological states similar to $MnBi_2Te_4$. For example, $EuBi_2Te_4$ is another AFM TI, and $MnSb_2Te_4$ is at the topological quantum critical point [46]. Actually, tetradymite-type compounds XBA_2B_3 belong to a large class of ternary chalcogenides materials $(XB)_n(A_2B_3)_m$ with $X = (\mathrm{Ge, Sn, or\ Pb})$, $A = (\mathrm{Sb\ or\ Bi})$, and $B = (\mathrm{Se\ or\ Te})$, most of which were found to be TIs [59]. Interestingly, $(GeTe)_n(Sb_2Te_3)_m$ and $(GeTe)_n(Bi_2Te_3)_m$ have been widely studied as phase change memory materials [60]. By tuning the layer index m and n, we can play with the crystal structure, the topological property, and the magnetic property of the series of materials $(XB)_n(A_2B_3)_m$, which opens a broad way to study emergent phenomena of magnetic topological states. For example, the dynamic axion field may be obtained in these systems.

Finally, the intrinsic magnetism and band inversion further lead to QAH effect in odd layer $MnBi_2Te_4$ thin film with $\mathcal{I}\Theta$ broken [46]. The intrinsic magnetic topological materials predicted here are simple and easy to control, which could host extremely rich topological quantum states in different spatial dimensions and are promising for investigating other exotic emergent particles such as Majorana fermions.

We thank Ke He for stimulating discussions. H. Z. is supported by the Natural Science Foundation of China

(Grants No. 11674165 and 11834006) and the Fok Ying-Tong Education Foundation of China (Grant No. 161006). J. W. is supported by the Natural Science Foundation of China through Grant No. 11774065, the National Key Research Program of China under Grant No. 2016YFA0300703, the Natural Science Foundation of Shanghai under Grant No. 17ZR1442500, the Open Research Fund Program of the State Key Laboratory of Low-Dimensional Quantum Physics through Contract No. KF201606, and by Fudan University Initiative Scientific Research Program. D. Z. and M. S. contributed equally to this work.

Note added.—Recently, we learned of the experimental papers in the same material by Gong *et al.* [61] and Otrokov *et al.* [62].

*zhanghj@nju.edu.cn
†wjingphys@fudan.edu.cn

[1] M. Z. Hasan and C. L. Kane, Rev. Mod. Phys. **82**, 3045 (2010).
[2] X.-L. Qi and S.-C. Zhang, Rev. Mod. Phys. **83**, 1057 (2011).
[3] C.-K. Chiu, J. C. Y. Teo, A. P. Schnyder, and S. Ryu, Rev. Mod. Phys. **88**, 035005 (2016).
[4] N. P. Armitage, E. J. Mele, and A. Vishwanath, Rev. Mod. Phys. **90**, 015001 (2018).
[5] C. L. Kane and E. J. Mele, Phys. Rev. Lett. **95**, 226801 (2005).
[6] B. A. Bernevig, T. L. Hughes, and S.-C. Zhang, Science **314**, 1757 (2006).
[7] M. König, S. Wiedmann, C. Brüne, A. Roth, H. Buhmann, L. Molenkamp, X.-L. Qi, and S.-C. Zhang, Science **318**, 766 (2007).
[8] X. Qian, J. Liu, L. Fu, and J. Li, Science **346**, 1344 (2014).
[9] Y. Xia, D. Qian, D. Hsieh, L. Wray, A. Pal, H. Lin, A. Bansil, D. Grauer, Y. S. Hor, R. J. Cava, and M. Z. Hasan, Nat. Phys. **5**, 398 (2009).
[10] H. Zhang, C.-X. Liu, X.-L. Qi, X. Dai, Z. Fang, and S.-C. Zhang, Nat. Phys. **5**, 438 (2009).
[11] Y. L. Chen, J. G. Analytis, J. H. Chu, Z. K. Liu, S. K. Mo, X. L. Qi, H. J. Zhang, D. H. Lu, X. Dai, Z. Fang, S. C. Zhang, I. R. Fisher, Z. Hussain, and Z. X. Shen, Science **325**, 178 (2009).
[12] H. Weng, C. Fang, Z. Fang, B. A. Bernevig, and X. Dai, Phys. Rev. X **5**, 011029 (2015).
[13] S.-M. Huang, S.-Y. Xu, I. Belopolski, C.-C. Lee, G. Chang, B. Wang, N. Alidoust, G. Bian, M. Neupane, C. Zhang, S. Jia, A. Bansil, H. Lin, and M. Z. Hasan, Nat. Commun. **6**, 7373 (2015).
[14] A. A. Soluyanov, D. Gresch, Z. Wang, Q. Wu, M. Troyer, X. Dai, and B. A. Bernevig, Nature (London) **527**, 495 (2015).
[15] S.-Y. Xu *et al.*, Science **349**, 613 (2015).
[16] B. Q. Lv, H. M. Weng, B. B. Fu, X. P. Wang, H. Miao, J. Ma, P. Richard, X. C. Huang, L. X. Zhao, G. F. Chen, Z. Fang, X. Dai, T. Qian, and H. Ding, Phys. Rev. X **5**, 031013 (2015).
[17] F.-F. Zhu, W.-J. Chen, Y. Xu, C.-L. Gao, D.-D. Guan, C.-H. Liu, D. Qian, S.-C. Zhang, and J.-F. Jia, Nat. Mater. **14**, 1020 (2015).
[18] L. Lu, J. D. Joannopoulos, and M. Soljačić, Nat. Photonics **8**, 821 (2014).
[19] J. Ruan, S.-K. Jian, H. Yao, H. Zhang, S.-C. Zhang, and D. Xing, Nat. Commun. **7**, 11136 (2016).
[20] B. Bradlyn, J. Cano, Z. Wang, M. G. Vergniory, C. Felser, R. J. Cava, and B. A. Bernevig, Science **353**, aaf5037 (2016).
[21] Z. Wang, A. Alexandradinata, R. J. Cava, and B. A. Bernevig, Nature (London) **532**, 189 (2016).
[22] B. Lv, Z.-L. Feng, Q.-N. Xu, X. Gao, J.-Z. Ma, L.-Y. Kong, P. Richard, Y.-B. Huang, V. Strocov, C. Fang *et al.*, Nature (London) **546**, 627 (2017).
[23] H. Zhou, C. Peng, Y. Yoon, C. W. Hsu, K. A. Nelson, L. Fu, J. D. Joannopoulos, M. Soljačić, and B. Zhen, Science **359**, 1009 (2018).
[24] S. Wu, V. Fatemi, Q. D. Gibson, K. Watanabe, T. Taniguchi, R. J. Cava, and P. Jarillo-Herrero, Science **359**, 76 (2018).
[25] T. Zhang, Y. Jiang, Z. Song, H. Huang, Y. He, Z. Fang, H. Weng, and C. Fang, Nature (London) **566**, 475 (2019).
[26] F. Tang, H. C. Po, A. Vishwanath, and X. Wan, Nature (London) **566**, 486 (2019).
[27] M. G. Vergniory, L. Elcoro, C. Felser, B. A. Bernevig, and Z. Wang, Nature (London) **566**, 480 (2019).
[28] C.-Z. Chang *et al.*, Science **340**, 167 (2013).
[29] R. S. K. Mong, A. M. Essin, and J. E. Moore, Phys. Rev. B **81**, 245209 (2010).
[30] X. Wan, A. M. Turner, A. Vishwanath, and S. Y. Savrasov, Phys. Rev. B **83**, 205101 (2011).
[31] G. Xu, H. Weng, Z. Wang, X. Dai, and Z. Fang, Phys. Rev. Lett. **107**, 186806 (2011).
[32] P. Tang, Q. Zhou, G. Xu, and S.-C. Zhang, Nat. Phys. **12**, 1100 (2016).
[33] G. Hua, S. Nie, Z. Song, R. Yu, G. Xu, and K. Yao, Phys. Rev. B **98**, 201116(R) (2018).
[34] X.-L. Qi, T. L. Hughes, and S.-C. Zhang, Phys. Rev. B **78**, 195424 (2008).
[35] L. Wu, M. Salehi, N. Koirala, J. Moon, S. Oh, and N. P. Armitage, Science **354**, 1124 (2016).
[36] J. Wang and S.-C. Zhang, Nat. Mater. **16**, 1062 (2017).
[37] R. Yu, W. Zhang, H.-J. Zhang, S.-C. Zhang, X. Dai, and Z. Fang, Science **329**, 61 (2010).
[38] J. Wang, B. Lian, and S.-C. Zhang, Phys. Scr. **T164**, 014003 (2015).
[39] L. Šmejkal, Y. Mokrousov, B. Yan, and A. H. MacDonald, Nat. Phys. **14**, 242 (2018).
[40] R. Li, J. Wang, X. L. Qi, and S. C. Zhang, Nat. Phys. **6**, 284 (2010).
[41] L. Šmejkal, J. Železný, J. Sinova, and T. Jungwirth, Phys. Rev. Lett. **118**, 106402 (2017).
[42] J. Wang, arXiv:1701.00896.
[43] H. Zhang, J. Wang, G. Xu, Y. Xu, and S.-C. Zhang, Phys. Rev. Lett. **112**, 096804 (2014).
[44] K. Kuroda, T. Tomita, M.-T. Suzuki, C. Bareille, A. Nugroho, P. Goswami, M. Ochi, M. Ikhlas, M. Nakayama, and S. Akebi *et al.*, Nat. Mater. **16**, 1090 (2017).
[45] D. S. Lee, T.-H. Kim, C.-H. Park, C.-Y. Chung, Y. S. Lim, W.-S. Seo, and H.-H. Park, CrystEngComm **15**, 5532 (2013).

[46] See Supplemental Material at http://link.aps.org/supplemental/10.1103/PhysRevLett.122.206401 for technical details on first-principles calculations and effective models with fitting parameters, which includes Refs. [47–48].
[47] G. Kresse and J. Hafner, Phys. Rev. B **47**, 558 (1993).
[48] G. Kresse and D. Joubert, Phys. Rev. B **59**, 1758 (1999).
[49] M. M. Otrokov, T. V. Menshchikova, M. G. Vergniory, I. P. Rusinov, A. Y. Vyazovskaya, Y. M. Koroteev, G. Bihlmayer, A. Ernst, P. M. Echenique, A. Arnau, and E. V. Chulkov, 2D Mater. **4**, 025082 (2017).
[50] L. Fu and C. L. Kane, Phys. Rev. B **76**, 045302 (2007).
[51] R. Yu, X. L. Qi, A. Bernevig, Z. Fang, and X. Dai, Phys. Rev. B **84**, 075119 (2011).
[52] A. M. Essin, J. E. Moore, and D. Vanderbilt, Phys. Rev. Lett. **102**, 146805 (2009).
[53] M. Mulligan and F. J. Burnell, Phys. Rev. B **88**, 085104 (2013).
[54] H.-G. Zirnstein and B. Rosenow, Phys. Rev. B **96**, 201112(R) (2017).
[55] J. Wang, B. Lian, X.-L. Qi, and S.-C. Zhang, Phys. Rev. B **92**, 081107(R) (2015).
[56] M. Mogi, M. Kawamura, R. Yoshimi, A. Tsukazaki, Y. Kozuka, N. Shirakawa, K. S. Takahashi, M. Kawasaki, and Y. Tokura, Nat. Mater. **16**, 516 (2017).
[57] D. Xiao, J. Jiang, J.-H. Shin, W. Wang, F. Wang, Y.-F. Zhao, C. Liu, W. Wu, M. H. W. Chan, N. Samarth, and C.-Z. Chang, Phys. Rev. Lett. **120**, 056801 (2018).
[58] K. Taguchi, T. Imaeda, T. Hajiri, T. Shiraishi, Y. Tanaka, N. Kitajima, and T. Naka, Phys. Rev. B **97**, 214409 (2018).
[59] H. Jin, J.-H. Song, A. J. Freeman, and M. G. Kanatzidis, Phys. Rev. B **83**, 041202(R) (2011).
[60] M. Wuttig and N. Yamada, Nat. Mater. **6**, 824 (2007).
[61] Y. Gong *et al.*, arXiv:1809.07926.
[62] M. M. Otrokov *et al.*, arXiv:1809.07389.